Hindawi
Advances in Multimedia
Volume 2022, Article ID 4405162, 9 pages
https://doi.org/10.1155/2022/4405162

Research Article

Study on Preparation and Properties of High-Strength Nano-Ceramic Coating on the Surface of Steel Structure Connectors

Hui Wang

Huainan Vocational and Technical College, Huainan 232001, China

Correspondence should be addressed to Hui Wang; wangtess1477@nuaa.edu.cn

Received 11 April 2022; Accepted 11 May 2022; Published 29 May 2022

Academic Editor: Qiangyi Li

In this paper, the preparation process of high-strength nano-ceramic coating on the surface of steel structure connectors is analyzed. By observing the surface morphology and internal defects of the ceramic coating, this paper analyzes the coating defects in combination with the coating deposition process. Moreover, this paper uses XRD to analyze the phase transition of the ceramic coating before and after spraying and tests the toughness of the coating, the adhesion between the coating and the reinforcement matrix, and the adhesion between the ceramic coating and the concrete. In addition, this paper studies its performance in combination with test research. The test results verify that the high-strength nano-ceramic coating on the surface of the steel structure connector has good performance.

1. Introduction

In recent years, the research and application of nano-ceramics have been paid more and more attention, and great progress has been made in the preparation of high-quality ceramic powders. However, how to make full use of these nanomaterials and how to give full play to the potential excellent properties of nano-ceramics are still problems to be solved. In the past, the application research of nano-ceramics mainly focused on the field of nano-ceramic bulk materials. Due to the high raw material cost of nano-powders, the application of bulk nanomaterials is limited to a certain extent. However, with the deepening of research, the research on nano-ceramic coatings has attracted extensive attention. The application of nano-ceramic coatings has opened up a new field for nano-ceramic materials. At present, the methods of preparing nano-ceramic coatings mainly include vapor deposition, thermal spraying technology, sol-gel method, and electrodeposition method. One of the most likely to produce market benefits in a short period of time is thermal spray technology. From the research status at home and abroad, there are many related reports on the preparation of nano-ceramic coatings by plasma spraying technology, and it is also the most likely thermal spraying nano-coating technology to be practical. The research and development of nano-ceramic structural coatings has received great attention from governments around the world, and the application of nano-coating materials has been listed as one of the key research directions of materials science during the "Tenth Five-Year Plan" period in China. Moreover, the preparation of nano-ceramic coatings by plasma spraying technology is an interdisciplinary technology. Due to the short development time, and because the coating performance has not fully met the coating design requirements, there is still a lot of room for development of nano-ceramic coatings prepared by plasma spraying technology. Therefore, it is believed that, in the near future, plasma sprayed nano-ceramic coatings will definitely play an important role in China's economic construction.

Ceramic materials have the characteristics of high hardness, high melting point, good thermal stability, and chemical stability. When used as a coating, it can effectively improve the wear resistance, high temperature resistance, high temperature oxidation resistance, thermal shock

resistance, corrosion resistance, and other properties of the complete material. Ceramic materials for thermal spraying can be roughly divided into two categories: oxide ceramics and cermets [1]. Oxides and composite oxides are the most widely used materials for preparing ceramic coatings. At present, the commonly used materials are oxide ceramics such as alumina-based, cobalt oxide-based, tin oxide-based, chromium oxide-based, magnesium oxide-based and special functional oxide ceramics, and mixtures of these ceramic materials [2]. The melting point of oxide ceramics is generally relatively high. In order to fully melt and obtain a dense coating, a higher temperature heat source is required. Therefore, the coating is usually prepared by plasma spraying technology. At the same time, oxide ceramics have stable performance and can be sprayed directly in the atmospheric environment without vacuum or protective atmosphere, which is of great benefit for equipment manufacturing, spraying workshop design, and cost reduction [3]. Therefore, oxide ceramics are the most widely used and most used ceramic coating materials in thermal spraying technology. In actual industrial production, alumina-based and zirconium oxide-based coating materials are the most commonly used, and as wear-resistant materials, they are also widely used in foreign countries to strengthen the blade of coating scrapers.

In this paper, the preparation process of high-strength nano-ceramic coating on the surface of steel structure connectors is analyzed, and its performance is studied in combination with testing research.

2. Related Work

With the development of nanotechnology and the in-depth research of nanomaterials, the improvement of human's understanding in the nanoscale range will open up a new level of human understanding of the world; secondly, nanotechnology will explore the frontier of science, integration of high-tech especially. The proposal and application of atomic-level and molecular-level processing technologies have greatly promoted the development of multiple disciplines, raising the ability of human beings to take nature up to an unprecedented new level [4]. The effective application of nanomaterials and structures with magnetic and other specific properties not only has a revolutionary impact on the information and biotechnology industries, but also promotes the technological upgrading of traditional industries [5]. Given the revolutionary impact of nanotechnology on Zhulai industry and the extensive technological transformation of traditional industries, many experts believe that new technologies centered on nanoscience and technology will become the dominant force in this century. At the same time, the research and application of nanoscience and technology has been regarded as the strategic goal of the new century, and huge human and financial resources have been invested [6].

Nanomaterials are an important foundation for the development of nanotechnology. Nanomaterials refer to materials whose geometric dimensions reach the nanoscale level and have special properties [7]. The preparation and research of nano-powder materials should include three aspects [8]: one is to systematically study the properties, microstructure, and spectral characteristics of nano-powder materials, and to find out the special characteristics of nano-powder materials by comparing them with conventional materials. The second is to improve the existing preparation process, and the preparation of high-performance nanomaterials is the direction of future efforts; the third is to develop new nanomaterials. Using mechanical grinding, the metal is evaporated and condensed and formed by in situ cold pressing. Many kinds of nanoparticles and powder materials have been prepared by methods such as amorphization and strong plastic deformation, and these preparation technologies are becoming more and more mature. Some have even reached industrialization, laying a good foundation for the application of nanomaterials [9]. At present, the key technical problem in the preparation and application of nano-powder materials is how to achieve homogenization, dispersion, and stabilization in the quality control of large-scale preparation. Until now. Many methods have been used to prepare nano-powder materials, but it is still difficult to develop a powder preparation technology with controllable, uniform, and cheap particle size [10].

The ultimate goal of nanotechnology is to create products with special functions starting from atoms and molecules. Therefore, the development and application level of nanodevices are an important sign of entering the nano-era [11]. The use of semiconducting nanotubes and metallic nanotubes to assemble carbon nanotubes with tunnel structure is likely to develop into a new type of nanodevices, especially new materials designed based on the principle of organization. It has a wide range of application prospects in magnetism and other aspects [12]. The research objects in this field are mainly nano-array systems, nano-mosaic systems, mesoporous and nanoparticle composite systems, and nanoparticle films. The purpose is to design new material systems according to needs and explore ways to improve material properties [13].

The surface structure and state of nano-powder materials have an important influence on the further application of nanomaterials. Nanoparticles cannot achieve nanoscale dispersion, and the performance of nanomaterials is difficult to fully reflect. Therefore, people have been carrying out hard exploration on nano-surface technology. Surface modification is an effective way to solve the growth and agglomeration of nanoparticles [14]. Studies have shown that if a certain substance is coated on the outer surface of nanometer or micrometer, its surface is modified or made into composite particles, and two kinds of nanoparticles or nanometer and micrometer particles with different properties are made into composite particles, which will be effective. The problem of agglomeration of single nanoparticles can be avoided, and the excellent characteristics of nanoparticles can be fully exerted to improve their use effect. In addition to the surface volume effect and quantum size effect of a single ultrafine particle, the

composite particle also has composite synergistic and multifunctional effects. It also improves the surface properties of a single particle and increases the contact area of two or more components to make it perform better [15]. Nanoparticles and microparticles are appropriately compounded. The prepared composite particles often not only have the properties of nanoparticles, but also make the micro-particles exhibit the properties of nanometers. This will greatly reduce the cost of using nanomaterials and improve the performance and added value of micron materials. Moreover, it solved the problem of difficulty in using nano-powders and opened up a new way to open up the application prospects of nanomaterials [16].

The sintering of nano-ceramics is different from the sintering of coarse-grained ceramics. The sintering of coarse-grained ceramics generally does not need to consider the growth of grains, while the sintering of nano-powders must not only maintain the nanometer size of the grains, but also consider full densification, in order to fully reflect many excellent properties of nano-ceramic materials [17]. Therefore, how to suppress the grain growth during the sintering process is a key issue in the sintering of nano-ceramic powders, and it has also become the most important issue in all researches on nano-ceramic sintering. Interfacial migration provides the basic conditions for grain growth. In a sense, inhibiting interfacial migration will prevent grain growth and improve thermal stability [18].

3. Test Materials and Methods

The Q235 steel commonly used in engineering is used as the base material in the test, and its chemical composition is shown in Table 1.

In the test, Al_20_3-13wt.%TiO2 (AT13) and Al_2O_3-40wt.% TiO_2 (AT40) ceramic powders are used as micron-scale coating materials, and the powder particle size ranged from 30 to 50 um. Al_2O_3-13wt.%TiO2 (nAT13) ceramics are used as the nanoscale coating material. The raw material powder is nanoparticles with high density and good fluidity. The average diameter of the agglomerated powder is 30 um. The microscopic morphology of each powder is shown in Figure 1. The AT13 and AT40 powders are irregular particles, and the nAT13 powder is spherical particles.

Between the working layer and the substrate, a bonding layer needs to be sprayed to improve the physical compatibility between the two and improve the bonding strength of the working layer. In this test, NiAI powder is used as the bonding layer material, which is a coated composite powder composed of Al powder as the core and fine nickel powder adhered around it. The powder particle size ranged from 40 to 75 um.

P.II 52.5 cement is used in the test, and its chemical composition and physical properties are shown in Tables 2 and 3 [19].

Class I fly ash is used in the test, and its chemical composition and technical indicators are shown in Table 4 and 5.

The test adopts continuous gradation of ordinary river sand, the fineness modulus is 2.62, the actual measured apparent density is 2630 kg/m^3, the mud content (mass fraction) is less than 1.5%, and the mud block content is less than 0.5%. During the use of river sand, a 4.75 mm square-hole sieve is used to sieve it, and the remainder of the sieve is removed. The gradation is shown in Table 6.

Table 1: Q235 steel composition (mass percentage).

Element	Content (%)	Element	Content (%)
C	0.141–0.222	S	≤0.052
Mn	0.302–0.651	P	≤0.0453
Si	≤0.303	Fe	Margin

The mixed water is used as clean tap water in the test.

The test uses polycarboxylate superplasticizer with a solid content of 40% and a water reduction rate greater than 40%. The use of superplasticizers can prepare high-performance concrete, effectively reduce unit water consumption, and improve the fluidity of fresh concrete.

The preparation water of the solution in the test is pure water, and the chemical information is shown in Table 7.

The volatile impurities such as water vapor contained in the spraying powder will be gasified at high temperature during the spraying process, resulting in the escape of gas, which will lead to an increase in the porosity of the coating. Moreover, the presence of these impurities will increase the viscosity of the powder and cause blockage in the process of powder transportation. Therefore, before spraying, NiAl metal powders and AT13, AT40, and nAT13 ceramic powders are placed in a DGG-9070B electric heating constant temperature blast drying oven at 70°C for preheating and drying for 6 h.

The surface of the rebar matrix should also be pretreated. Due to the black oxide scale and a certain number of pitting pits on the surface of the Q235 steel bar, a simple polishing treatment is required on the surface of the steel bar. Grinding the steel bar surface with a hand-held grinder and a louver can effectively remove the oxide scale and smooth the pitting pit and finally obtain a smooth silver-white steel bar surface. Secondly, the sprayed surface of the polished steel bar matrix is sandblasted and roughened in a 9080A type sandblasting machine using alumina sandblasting with a particle size of 16 mesh.

Coated steel bars are prepared by plasma spraying of Q235 smooth round bars with sizes of 10 mm and 25 mm in the experiment. According to the ASTM C633-01 standard for the bonding strength of thermal spray coatings of the American Society for Testing and Materials, the coating is sprayed on the @25 mm × 30 mm cylindrical section to prepare the bond strength test specimen, as shown in Figure 2.

The plasma sprayed sample is composed of substrate, bonding layer, and working layer. Argon gas is used as the main gas and carrier gas for spraying, and helium gas is used as auxiliary gas. The spraying process parameters are shown in Table 8.

First, the coated steel bars are immersed in a simulated concrete pore solution of pH 13.5 for 3 d to remove the metastable phase on the surface of the coating. After that, it is washed with deionized water and dried, then air-dried, and then sealed.

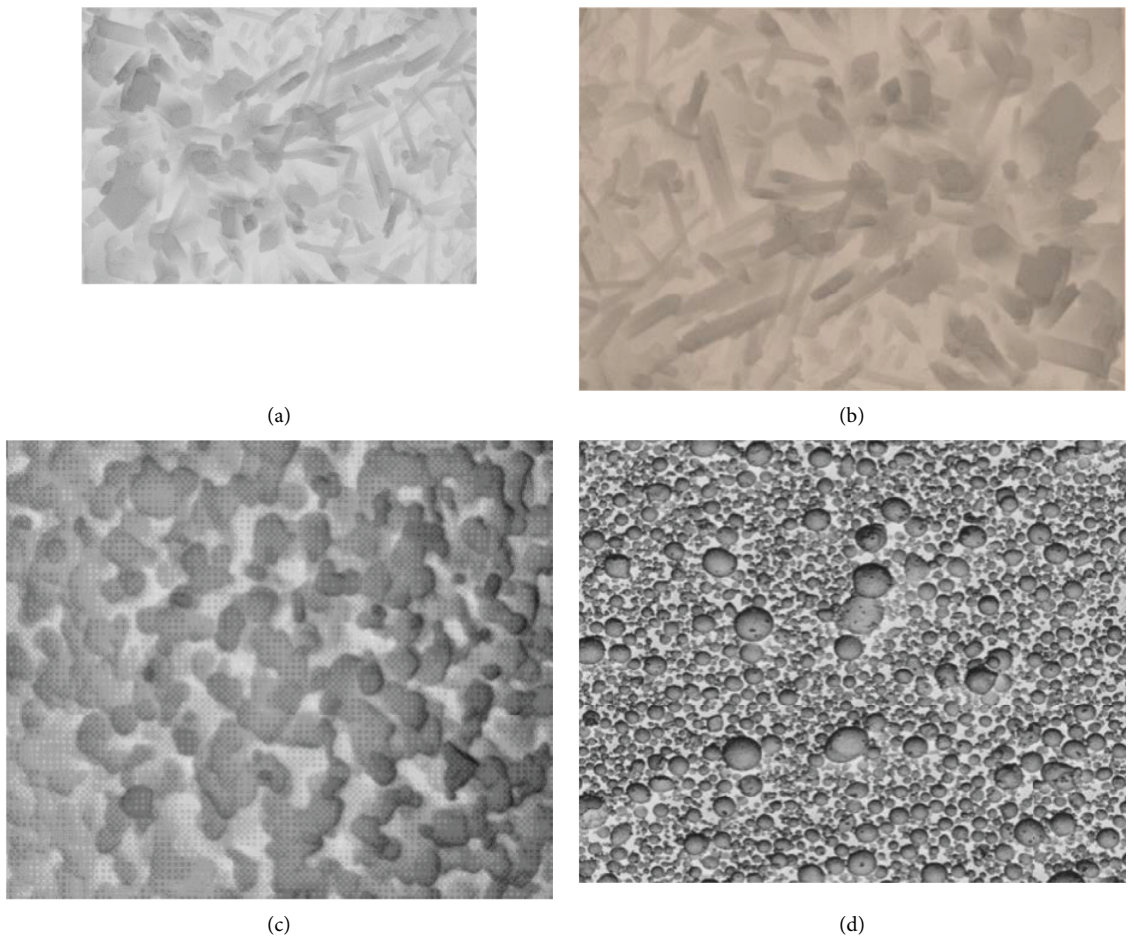

(a) (b) (c) (d)

Figure 1: Micromorphology of ceramic powder. (a) AT13. (b) AT40. (c) nAT13. (d) Nanoscale AT13.

Table 2: Cement chemical composition (mass fraction).

Chemical composition	Content (%)	Chemical composition	Content (%)
CaO	65.347	Mgo	0.8787
siO_2	20.604	SO_3	1.8988
Al_2O_3	4.747	Other	3.2724
Fe_2O_3	3.4138		

Table 3: Basic physical properties of cement.

Specific surface area (m^2/kg)	362.41	
Standard consistency water consumption (%)	24.82	
80um sieve balance (%)	0.22	
Coagulation time (min)	Initial setting	141.4
	Final coagulation	247.45
Flexural strength (MPa)	3D	7.272
	28D	10.706
Compressive strength (MPa)	3D	34.542
	28D	63.428

Before sealing, nano-SiO2 modified polyurethane (PU), curing agent, and diluent are mixed and stirred in a precision booster for 30 minutes at a stirring speed of 3000 r/min to obtain a sealing agent. Then, a conventional dipping process

Table 4: Chemical composition of fly ash (mass score).

Chemical composition	Content (%)	Chemical composition	Content (%)
SiO_2	50.4596	K_2O	0.9898
Al_2O_3	33.3502	MgO	1.1817
Fe_2O_3	4.5652	Na_2O	0.6666
CaO	66.7509	SO_3	1.8988

Table 5: Technical indicators and test results of fly ash.

Serial number	Test items	Standard indicator			Test results
		I	II	III	
1	Fineness (45 um sieve residue) %	≤12.00	≤25.00	≤45.0	4.61
2	Water demand ratio (%)	≤950	≤105.0	≤115.0	922
3	Loss on ignition (%)	≤5.00	≤8.000		3.11
4	Moisture content (%)		≤1.00		0.22
5	Free calcium oxide		1		1.21
6	Total alkali content				1.57
7	Apparent density (kg/m)				2240.2
8	Specific surface area (m^3/kg)				454.2
9	Activity index			70	73

Table 6: River sand grading.

Sieve size (mm)	Cumulative sieve residue (%)	Sieve size (mm)	Cumulative sieve residue (%)
4.7975	1.9695	0.606	45.9752
2.3836	9.1203	0.303	86.0419
1.1918	29.0173	0.1515	99.5456

Table 7: Chemical information.

Chemical	Purity	Molecular weight	Chemical	Purity	Molecular weight
$Ca(OH)_2$	Analytically pure	70.7909	Epoxy resin	—	—
KOH	Analytically pure	56.6711	Polyamide resin	—	—
NaOH	Analytically pure	40.4	E-7 glue	—	—
NaCl	Analytically pure	59.0244	Nano-modified polyurethane	—	—

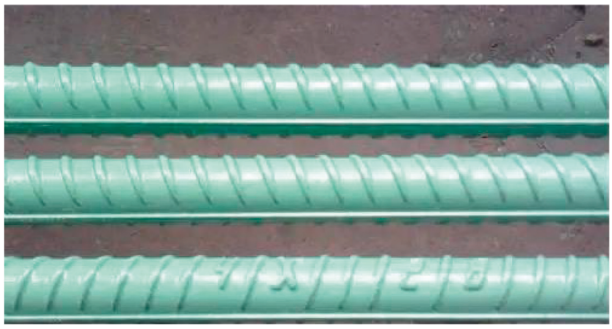

Figure 2: Coated reinforcement.

Table 8: Spraying parameters.

Coating type	NiAl	AT13	AT40	nAT13
Current (A)	650.00	750.00	750.00	750.00
Voltage (V)	46.00	47.00	47.00	47.00
Main gas (Ar) (psi)	60.00	60.00	60.00	60.00
Auxiliary gas (He) (psi)	50.00	50.00	50.00	50.00
Carrier gas (Ar) (psi)	40.00	40.00	40.00	40.00
Spray distance (mm)	100.00	100.00	100.00	100.00

is employed. The sample is soaked in the sealing agent for 20 minutes and then taken out. The surface bubbles are broken by brushing, so that the sealing agent could better penetrate into the coating. After brushing, it is soaked for 20 minutes, and the above operation was repeated. After repeated immersion and brushing, the samples were cured at room temperature for 24 hours, and relevant tests were carried out after curing.

The concrete used in the test is the concrete with the strength grade of C50, the concrete water-binder ratio is 0.35, and the mixing ratio is shown in Table 9.

In the test, the mixed concrete needs to have high fluidity. The formed concrete is released from the mold and sent to the standard curing room and is ready for use after curing for 28 days.

Ceramic materials are brittle and sensitive to stress and cracks. When the matrix material undergoes large plastic deformation, the ceramic coating is prone to brittle fracture. In order to test the toughness of the ceramic coating, the three-point bending method is used to make the substrate

Table 9: Concrete mix ratio.

Raw materials	Mix ratio (kg/m3)	Raw materials	Mix ratio (kg/m3)
Cement	315.00	Stone	1076.00
Fly ash	135.00	Water	157.50
Sand	717.00	Water reducer	0.5–0.7%

produce a large plastic deformation, and the failure mode of the coating is observed at the deformation point.

The test uses a 25 mm surface coated steel bar sample, which is loaded on a CMT 5105 electronic universal testing machine. The steel bars are placed on two fulcrums with a distance of 20 cm, the loading point is located in the middle of the fulcrum, and the loading is controlled by displacement, and the loading speed is 0.02 mm/s.

The loading speed of the test is 0.02 mm/s, and the loading force when the sample breaks is recorded. In order to prevent the eccentric load or the specimen from being affected by the bending moment during the tensile process, an automatic calibration device is made according to the relevant instructions in ASTM C633-01. The butt-jointed bond strength test specimens are assembled in an automatic calibration device, as shown in Figure 3.

Due to the action of gravity, the coarse and fine aggregates in the uncoagulated and hardened concrete will be deposited, and the cohesion force of the bottom and top of the concrete to the steel bars will be inhomogeneous, the cohesion force will decrease from bottom to top, and there will be sudden changes at the boundary. The upper and lower ends of the steel bars embedded in the concrete are covered with 20 mm PVC pipes, respectively, and the holes are reserved, so that the formed steel bars do not contact the concrete, and the steel bars only contact the concrete in the middle part of the specimen. The size of the sample is shown in Figure 4.

Since each substance has a specific unit cell size and lattice type, the position of each atom is also certain, and the diffraction pattern of the material is determined. Therefore, the X-ray diffraction pattern of the crystal can easily and qualitatively detect the analyte phase. The interplanar spacing d and its relative intensity I calculated according to the angular position of each line of the diffraction pattern are inherent characteristics of the crystal. The d value and I/

Figure 3: Bonding force tensile test.

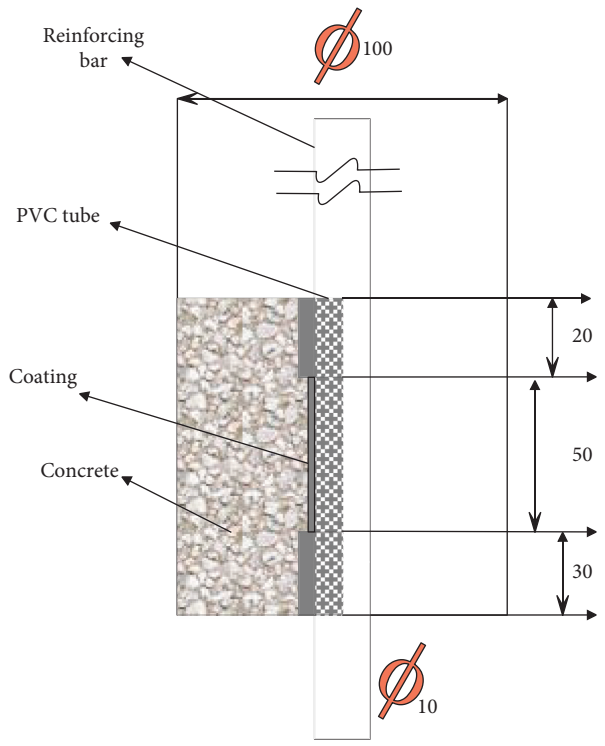

Figure 4: Reinforced concrete sample (unit: mm).

given by the diffraction pattern of the unknown crystal are compared with the crystal structure of the known substance, and if they are consistent, the phase structure of the substance can be determined.

The powders of AT13, AT40, and nAT13 and the sprayed coating were used as the X-ray irradiation surface, respectively. Using the step scanning method, from 10° to 90° with a step width of 0.05°, the diffraction intensity corresponding to each 20 angle is measured. The results are analyzed by phase analysis using MDI Jade 5 analysis software.

In the test, a section of 25 mm coated steel bar was cut, and the cross section of the steel bar is polished with 400#, 600#, 800#, and 1000# sandpaper, respectively, and then polished with diamond liquid. The microstructure, internal defects, and coating thickness of the coating are observed by scanning electron microscope (SEM).

The 25 mm steel bar with the coating on the surface was cut into several cylinders with a length of 10 mm by wire cutting, and then the section of the cylinder was equally divided into 6 parts to obtain 6 sectors. The coating is located on the surface of the polyhedron, which can realistically simulate the surface environment where the coating is located in the test instead of the plane. The copper wire is wrapped around the noncoated surface and reinforced with solder to ensure that the copper wire and the sample are in good electrical conductivity.

During the test, it is necessary to ensure that the coating surface is in contact with the solution, and the other surfaces are isolated from the solution. Therefore, the samples were sealed with epoxy resin. First, the sample to be connected with the copper wire is placed in a special cylindrical mold. Secondly, it is necessary to prepare epoxy resin with good fluidity, pour it into the mold after stirring evenly, make sure that the epoxy resin fills the mold, and cure it at room temperature for 24 hours. Finally, after the epoxy resin is fully cured, the mold is removed, and the epoxy resin covering the coating surface is removed, so that the coating surface is exposed, and the exposed area is kept about 1 cm^2.

The mother liquors used in the experiments were all simulating concrete pore solutions. By adding different contents of CI and changing the pH value of the solution, the effects of CI concentration and pH value on the corrosion behavior of the coating were investigated. The substances

Table 10: Composition of simulated concrete pore solution (mol/L).

Serial number	Ca $(OH)_2$	NaOH	KOH	NaCl
pH13.5-CI0	0.0303	0.202	0.505	
pH13.5-C10.25	0.0303	0.202	0.505	0.2525
pH13.5-C10.5	0.0303	0.202	0.505	0.505
pH13.5-C11.0	0.0303	0.202	0.505	1.01
pH12.5	0.002424	0.0202	0.0505	
pH12.5	0.0002424	0.00202	0.00505	

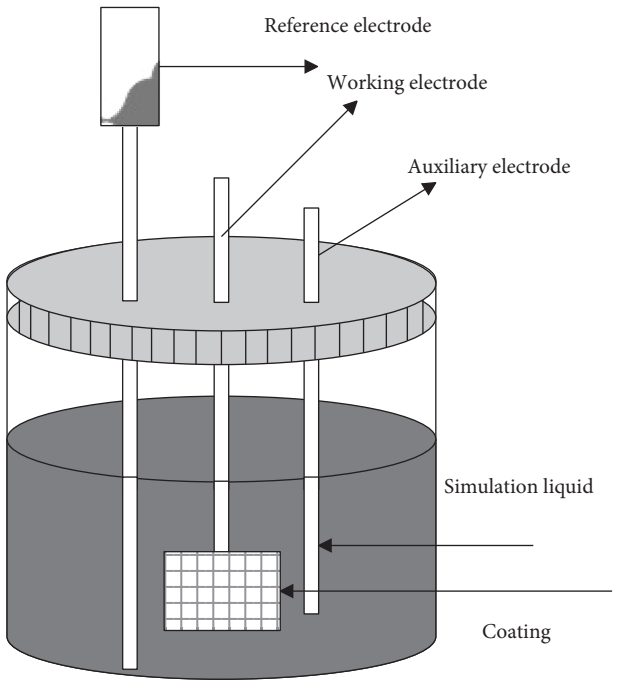

Figure 5: Electrochemical test system.

contained in each solution and their contents are shown in Table 10, and the ambient temperature for solution preparation and storage is 25°C.

The corrosion behavior of the coating is studied by electrochemical method. The electrochemical test was carried out using a PARSTAT4000 electrochemical workstation produced by Princeton and a three-electrode system. As shown in Figure 5, the test system is carried out at room temperature of 25°C.

3.1. Working Electrode. The electrode measured in the test is the working electrode. During the test, it can generate the corresponding electrochemical reaction and feedback the response signal. The working electrodes in this test are AT13, AT40, and nAT13 ceramic coatings, respectively.

3.2. Auxiliary Electrode. In the electrochemical system, the electrode immersed in the same solution to conduct the current of the tested electrode back to the external power source is the auxiliary electrode, which forms a closed current loop with the working electrode. In order to prevent the auxiliary electrode from reacting with the electrolyte solution and the cell voltage fluctuation caused by electrode polarization, nonpolarized or difficult-to-polarize materials are usually used as auxiliary electrodes, such as platinum and graphite.

3.3. Reference Electrode. The reference electrode refers to an electrode of known potential that is close to ideal and unpolarized. During the electrochemical test, the reference electrode is substantially free of current and is used to determine the working electrode potential relative to the reference electrode. An ideal reference electrode should have the following characteristics: the electrode reaction on the electrode surface should be reversible. The reproducibility of the potential is good, the electrode potential is stable, and the drift with time is small. The electrode changes with temperature, and the potential does not produce hysteresis. The electrode structure is firm, stable in nature, convenient to use, and easy to maintain.

The calomel electrode is commonly used as a reference electrode in the laboratory, and its electrode reaction is

$$Hg_2Cl_2 + 2e^- \rightleftharpoons 2Hg + 2Cl^-. \quad (1)$$

Its potential is related to the Cl^- concentration. Usually, the concentration of Cr is 0.1 molL, 1 mol/L, and saturated. When the concentration of KCI is saturated, it becomes a saturated calomel electrode. The kinetic information of the corrosion process on the electrode material can be obtained by measuring the polarization curve. The main one is to obtain information on the corrosion rate of the material. Secondly, for the electrode material in the corrosion active zone, it is also desirable to obtain other kinetic information of the electrode corrosion reaction, such as the Tafel slope of the anodic and cathodic reactions and the limiting diffusion current density of the depolarization. The corrosion current density i_{corr} and corrosion potential E_{corr} of the electrode material can be obtained by the polarization curve epitaxy method in the strongly polarized region, namely, the Tafel epitaxy method.

The anodic current density i_A and cathodic current density i_C outside the corrosion electrode are shown in (2) and (3):

$$i_A = i_{\text{corr}}\left[\exp\frac{2.3\Delta E}{b_a} - \exp\left(-\frac{2.3\Delta E}{b_c}\right)\right]. \quad (2)$$

$$i_A = i_{\text{corr}}\left[\exp\left(-\frac{2.3\Delta E}{b_c}\right) - \exp\frac{2.3\Delta E}{b_a}\right]. \quad (3)$$

Among them, ΔE is the difference between the outside potential and the electrode corrosion potential, that is, the polarization value. b_a and b_c are the Tafel slopes of common logarithms for anodic and cathodic reactions, respectively.

When the absolute value of the polarization value is

$$|\Delta E|\frac{2b_a b_c}{b_a + b_c}. \quad (4)$$

the electrode material enters the strongly polarized region. At this time, the real polarization curve coincides with the ideal polarization curve in a straight line.

After entering the strong anodic polarization region, the current density of the cathodic reaction can be neglected, and the relationship between the current density of the outer anode and the polarization value is

$$i_C = i_{\text{corr}} \exp \frac{2.3\Delta E}{b_a}, \quad \Delta E = b_a \lg i_A - b_c \lg i_{\text{corr}}. \tag{5}$$

After entering the strong cathodic polarization region, the current density of the anodic reaction can be ignored, and the relationship between the outer cathodic current density and the polarization value is

$$i_C = i_{\text{corr}} \exp\left(-\frac{2.3\Delta E}{b_a}\right), \quad \Delta E = -b_c \lg|i_C| + b_a \lg i_{\text{corr}}. \tag{6}$$

Therefore, in the strongly polarized region, a straight line is drawn for ΔE and lgi, respectively, and the corresponding corrosion current density can be obtained at the intersection of the straight lines.

4. Analysis and Discussion

XRD is used to analyze the phase transition of the ceramic coating before and after spraying, and the toughness of the coating, the adhesion between the coating and the reinforcement matrix, and the adhesion between the ceramic coating and the concrete are tested. In this paper, the electrochemical properties and potentiodynamic polarization curves of steel bars treated by different methods at different immersion periods were detected by electrochemical impedance spectroscopy, and the corrosion current and corrosion potential of steel bars after immersion were investigated. Through the equivalent circuit fitting of electrochemical impedance spectroscopy, macroscopic morphology observation and microscopic analysis after immersion, the corrosion resistance, and corrosion behavior mechanism of ATl3, AT40, and nATl3 ceramic-coated steel bars in simulated concrete pore solutions with different pH values and different chloride ion concentrations were studied, respectively. For the problems of reduced concrete cohesion and the diffusion channel provided by defective chloride ions in the coating, the weak performance of the coating is improved by impregnation with an organic pore-sealing agent. The following main conclusions are obtained: (1) the surface of micron ATl3 and AT40 ceramic coatings has obvious lamellar accumulation morphology, and there are microcracks on the surface of ATl3 coating; the melted particles of nATl3 coating are closely combined, forming a relatively uniform whole on the surface; the content of pores in ATl3 and AT40 coatings is higher, and the pore size is larger, and the porosity of ATl3 is higher than that of AT40; the interior of nATl3 is relatively dense, with less pore content and smaller size. (2) The toughness of ceramic coating is nATl3>ATl3>AT40 from good to bad. The damage of the coating is mainly due to the expansion of cracks in the coating, and the existence of nanoparticles in nATl3 can effectively hinder the expansion of cracks, so the toughness is improved.

5. Conclusion

It is manifested as high strength and high shear, high specific heat, high thermal expansion rate, high electrical conductivity, high magnetic permeability, etc. and has become an important research field in the frontier of scientific and technological development in the new century. The combination of nanomaterials and spraying technology to prepare composite coatings containing nanostructures can improve the modification effect of surface technology. The thermal spraying process is simple, the selection range of coating and substrate is large, the coating thickness variation range is large, the deposition rate is high, and it is easy to form a composite coating. Compared with traditional coatings, nanostructured coatings have significant improvements in strength, toughness, wear resistance, corrosion resistance, thermal barrier, etc., and some coatings can have the above-mentioned properties at the same time. In this paper, the preparation process of the high-strength nano-ceramic coating on the surface of the steel structure connector is analyzed, and the performance of the high-strength nano-ceramic coating on the surface of the steel structure connector is analyzed, and the performance of the high-strength nano-ceramic coating is verified by the experimental study.

Data Availability

The labeled dataset used to support the findings of this study is available from the corresponding author upon request.

Conflicts of Interest

The author declares no competing interests.

Acknowledgments

The research is supported by Anhui Province Outstanding Top-Notch Talents Training funding project—Domestic Visiting and Training program for outstanding young backbone teachers in colleges and universities (gxgnfx2020145); and Key project of Natural Science Research in Universities of Anhui Province—Research on remanufacturing method and key Technology of waste equipment in coal industry (KJ2021A1580).

References

[1] Y. Wang, H. Xia, and X. Yuan, "Distributed defect recognition on steel surfaces using an improved random forest algorithm with optimal multi-feature-set fusion," *Multimedia Tools and Applications*, vol. 77, no. 13, Article ID 16741, 2018.

[2] Z. Mentouri, A. Moussaoui, and D. Boudjehem, "Steel strip surface defect identification using multiresolution binarized image features," *Journal of Failure Analysis and Prevention*, vol. 20, no. 6, pp. 1917–1927, 2020.

[3] Z. Peng, X. U. Ke, and Y. Chaolin, "Surface defect recognition for moderately thick plates based on a SIFT operator," *Journal of Tsinghua University*, vol. 58, no. 10, pp. 881–887, 2018.

[4] Q. Luo, X. Fang, and L. Liu, "Automated visual defect detection for flat steel surface: a survey," *IEEE Transactions on Instrumentation and Measurement*, vol. 69, no. 3, pp. 626–644, 2020.

[5] J. Li, Z. Su, and J. Geng, "Real-time detection of steel strip surface defects based on improved yolo detection network," *IFAC-PapersOnLine*, vol. 51, no. 21, pp. 76–81, 2018.

[6] H. Wang, S. Wei, and R. Huang, "Recognition of plate identification numbers using convolution neural network and character distribution rules," *ISIJ International*, vol. 59, no. 11, pp. 2044–2051, 2019.

[7] R. Hao, B. Lu, and Y. Cheng, "A steel surface defect inspection approach towards smart industrial monitoring," *Journal of Intelligent Manufacturing*, vol. 32, no. 7, pp. 1833–1843, 2021.

[8] J. Liu, G. Xu, and L. Ren, "Defect intelligent identification in resistance spot welding ultrasonic detection based on wavelet packet and neural network," *International Journal of Advanced Manufacturing Technology*, vol. 90, no. 9, pp. 2581–2588, 2017.

[9] J. Zhang, X. Kang, and H. Ni, "Surface defect detection of steel strips based on classification priority YOLOv3-dense network," *Ironmaking and Steelmaking*, vol. 48, no. 5, pp. 547–558, 2021.

[10] J. D. Kothari, "Detecting welding defects in steel plates using machine learning and computer vision algorithms," *International Journal of Advanced Research in Electrical, Electronics and Instrumentation Engineering*, vol. 7, no. 9, pp. 3682–3686, 2018.

[11] P. P. Sarkar, S. K. Dhua, and S. K. Thakur, "Analysis of the surface defects in a hot-rolled low-carbon C–Mn steel plate," *Journal of Failure Analysis and Prevention*, vol. 17, no. 3, pp. 545–553, 2017.

[12] M. H. Yao and Q. L. Gu, "A sparse representation method for image-based surface defect detection," *Optoelectronics Letters*, vol. 14, no. 6, pp. 476–480, 2018.

[13] E. D. Cho and G. B. Kim, "A study on illumination mechanism of steel plate inspection using wavelet synthetic images," *Journal of the Semiconductor & Display Technology*, vol. 17, no. 2, pp. 26–31, 2018.

[14] A. Anvar and Y. I. Cho, "Automatic metallic surface defect detection using ShuffleDefectNet," *Journal of The Korea Society of Computer and Information*, vol. 25, no. 3, pp. 19–26, 2020.

[15] B. Li, Z. Zhang, and H. Liu, "Characteristics and evolution of the spot segregations and banded defects in high strength corrosion resistant tube steel," *Acta Metallurgica Sinica*, vol. 55, no. 6, pp. 762–772, 2019.

[16] Y. Chen, H. W. Ma, and M. Dong, "Automatic classification of welding defects from ultrasonic signals using an SVM-based RBF neural network approach," *Insight-Non-Destructive Testing and Condition Monitoring*, vol. 60, no. 4, pp. 194–199, 2018.

[17] S. J. Kim and G. B. Kim, "A study on the defect classification of low-contrast· uneven· featureless surface using wavelet transform and support vector machine," *Journal of the Semiconductor & Display Technology*, vol. 19, no. 3, pp. 1–6, 2020.

[18] Z. Liu, J. Yao, and C. He, "Development of a bidirectional-excitation eddy-current sensor with magnetic shielding: detection of subsurface defects in stainless steel," *IEEE Sensors Journal*, vol. 18, no. 15, pp. 6203–6216, 2018.

[19] Y. Feng, K. Li, and Y. Gao, "Shaft surface defect detection method based on feature and morphology reconstruction," *Journal of Zhejiang University*, vol. 54, no. 3, pp. 427–434, 2020.